Available online at www.sciencedirect.com

ScienceDirect

Underground Space 27 (2026) 406–423

www.keaipublishing.com/undsp

Research Paper

A bar explosion model based on continuous–discontinuous element method and its application in blasting excavation

Yunpeng Li [a,b,d], Xinguang Zhu [d], Dong Chen [c], Jun Fu [c], Minjie Wen [a], Yiming Zhang [a,b,*]

[a] School of Civil and Transportation Engineering, Hebei University of Technology, Tianjin 300401, China
[b] School of Civil Engineering and Architecture, Zhejiang Sci-Tech University, Hangzhou 310018, China
[c] Third Engineering Co., Ltd., China Railway 16th Bureau Group, Huzhou 313002, China
[d] Key Laboratory for Mechanics in Fluid Solid Coupling Systems, Institute of Mechanics, Chinese Academy of Sciences, Beijing 100190, China

Received 7 July 2025; received in revised form 10 November 2025; accepted 1 December 2025
Available online 4 March 2026

Abstract

Blasting excavation is widely used in engineering, often involving complex whole layouts. However, the small size of the blasthole and the large size of the three-dimensional (3D) numerical model lead to the large calculation scale of the 3D blasting numerical simulation, which requires considerable calculation time. Typically, a 3D numerical model is simplified into a two-dimensional (2D) numerical model, and a 1/2- or 1/4-scale model can be adopted to reduce the calculation scale. To solve this problem, a one-dimensional bar explosion model is adopted to replace the traditional solid explosion model under the framework of the continuous–discontinuous element method. The detonation pressure is directly distributed to the elements penetrated by the bar, and the volume expansion of the elements is used to calculate the volume expansion attenuation detonation pressure at each stage of detonation, thus avoiding the problem of local mesh refinement. Compared with the solid explosion case, the reliability of the bar explosion model is verified by the propagation of the explosion stress wave, peak explosion pressure, and damage nephogram. In combination with the engineering background, three blasting conditions are simulated, and the optimal one is evaluated based on fracture degree and blast fragment size pass rate.

Keywords: Bar explosion model; Continuous–discontinuous element method (CDEM); Blasting excavation; Numerical simulation

1 Introduction

At present, urban transportation networks are well established, and large-scale transportation engineering projects are located mostly in mountainous areas. Compared with construction in flatlands, construction in mountainous areas is more challenging due to the presence of dense and high-strength rock formations. Furthermore, construction sites in these regions often encounter obstacles such as steep gradients, limited workspaces, and slippery and uneven construction paths, which make the excavation of foundation pits particularly difficult without the support of large-scale machinery. Blasting excavation is widely used because of its low cost and simple operability. However, blasting excavation often has strong uncertainty, and blasting can easily damage and crack the rock surrounding the foundation pit. Therefore, it is necessary to accurately control the range and degree of blasting damage.

Blasting tests carry significant potential safety risks and entail high experimental costs. Additionally, these experiments generate widespread dust, making it difficult for conventional testing instruments and optical devices to evaluate the characteristics of the explosion process. Furthermore, blasting involves complex dynamics that are affected by the coupling of stress, temperature, and fluid fields, posing a great challenge for theoretical research. As a result, most scholars currently rely on indoor dynamic tests such as drop hammer tests (Murali et al., 2024), split Hopkinson pressure bar (SHPB) tests (Asadi et al., 2023),

* Corresponding author at: School of Civil and Transportation Engineering, Hebei University of Technology, Tianjin 300401, China.
E-mail address: yiming.zhang@zstu.edu.cn (Y. Zhang).
Peer review under the responsibility of Tongji University

https://doi.org/10.1016/j.undsp.2025.12.004

and numerical simulations to conduct related studies. The finite-discrete element method (FDEM) develops governing equations based on energy principles (Munjiza, 2004; Munjiza et al., 2013). Han et al. (2020) used the FDEM to explore the damage evolution of deep rock after bench blasting, concluding that the explosive pressure is governed by the decoupling ratio of the blasthole. Sharafisafa et al. (2025) used the FDEM to study the blasting mechanism of jointed rock, demonstrating that the orientation of joints can change the rock failure pattern. Lu et al. (2024) explored the mechanism of crack propagation in the process of double-hole blasting via the combined FDEM and analysed the influences of different in situ stress conditions and whole spacings on the cracks between blastholes. Fan et al. (2016) used the peridynamics-smoothed particle hydrodynamics (PD-SPH) coupling method to simulate the blasting process of buried explosives in soil and verified the accuracy of the method through experiments.

These studies indicate that as scholars further explore the field of blasting, uncoupled methods are no longer sufficient to accurately describe the dynamic impact process; in addition, coupled continuous and discontinuous methods are often employed for research. Aside from the limitations of numerical methods, these blasting studies employ different levels of simplification. For example, these scholars have used the strategies of applying an equivalent explosive load, simplifying the model into a two-dimensional (2D) model, and adopting a three-dimensional (3D) model that is divided into hundreds of thousands or even millions of elements. On the one hand, these strategies reduce the accuracy of numerical simulations; on the other hand, they significantly increase the computational time. Thus, some scholars have adopted different strategies to speed up the solution. Fukuda et al. (2019) developed the parallel acceleration code of FDEM using the compute unified device architecture (CUDA) framework based on general-purpose computing on graphics processing units (GPGPU) and applied it to a single-hole blasting case. Benchmarks indicated a speed-up exceeding 128x. Durand et al. (2012) implemented a graphics processing unit (GPU)-based parallel acceleration of the discrete element method (DEM) and simulated the penetration of a concrete target. Liu et al. (2020) also developed the CUDA FDEM parallel program, which mainly optimizes the contact detection in parallel, and the overall acceleration ratio reaches 53x. Huang et al. (2025) used the OpenMP algorithm to accelerate the peridynamics-smoothed particle hydrodynamics (PD-SPH) coupling model, and the acceleration ratio of the code was 3.2x by simulating a soil blast with 2 million particles.

In terms of explosion load application, two main strategies are used to apply the explosive load. One strategy involves establishing solid explosive elements and uses the Jones–Wilkins–Lee (JWL) model to describe the detonation process. This method is used in commercial software such as Livermore Software Technology Corporation's dynamic analyzer (LS-DYNA) (Yin et al., 2025) and advanced simulation for engineering and sciences (ABAQUS) (Saifi et al., 2024). The other strategy is to input an equivalent time-history curve of the explosion load, which directly transfers the detonation pressure to the elements in the blasthole wall area. Common equivalent methods include the triangular load method (Park et al., 2009) and the impulse load method (Zhou et al., 2024). The former strategy involves establishing solid explosive elements, which inevitably leads to excessive refinement of the mesh near the blasthole and greatly increases the number of calculations, especially in 3D cases. The latter approach avoids local over-refinement by inputting an equivalent explosion load curve. However, for cylindrical charge cases, the long charge length indicates that the entire blasthole wall area elements should not be subjected to the same explosion load curve, as there is a blasting delay among different elements. Moreover, the core problem of the equivalent load is that the parameters are difficult to obtain, and the quality of the parameters directly affects the blasting effect. By comparing these two strategies, the advantages of the one-dimensional (1D) bar explosion model adopted in this work are as follows.

(1) The adopted 1D bar explosion model does not need to establish solid explosive elements, mitigating the need for excessive refinement of the element in the blasthole area, thereby significantly reducing the number of calculations.
(2) The detonation pressure of the bar-explosion model is calculated using the Landau model. Compared with the equivalent load method, the parameters are easier to obtain.
(3) The bar explosion model is used to attenuate the peak load in real time by calculating the volume expansion level of the element it penetrates, which is more consistent with the characteristics of bar-shaped explosion cases.

In this work, we employ the bar explosion model to apply the explosive load, aiming to avoid excessive mesh refinement near the blasthole, which can otherwise lead to a surge in the number of meshes. We conduct numerical simulations of blasting excavation of foundation pits using the continuous–discontinuous element method (CDEM), which is a numerical method that combines the finite and discrete element methods (Feng et al., 2014; Zhu et al., 2021). This approach can reasonably describe the whole process of rock evolution from continuous deformation, cracking, and crushing to scattering during the explosion process. This method has been widely used in the engineering blasting field (Li et al., 2022, 2023, 2024).

2 Computational method and bar explosion model

2.1 CDEM computing framework

The CDEM is a combined finite-discrete element method with an explicit time-integration algorithm. The governing equation is given as follows:

$$\frac{\mathrm{d}}{\mathrm{d}t}\left(\frac{\partial L}{\partial \dot{u}_i}\right) - \frac{\partial L}{\partial u_i} = Q_i, \tag{1}$$

$$L = \prod_{\mathrm{m}} + \prod_{\mathrm{e}} + \prod_{\mathrm{f}}, \tag{2}$$

where the subscript i is the node ID; Q_i is the force; u_i is the nodal displacement of the block element; $\dot{u}_i$ is the nodal velocity of the block element; L is the Lagrangian, which is the sum of the $\prod_{\mathrm{m}}$ kinetic energy, $\prod_{\mathrm{e}}$ deformation energy and $\prod_{\mathrm{f}}$ work done by conservative forces. For a domain Ω and its boundary S, $Q_i = Q_{\mu\mathrm{d}} + Q_{\bar{\mathrm{T}}}$, where $Q_{\mu\mathrm{d}}$ is the damping force and $Q_{\bar{\mathrm{T}}}$ is the external boundary force.

$$Q_{\mu\mathrm{d}} = \int_{\Omega} \mu_{\mathrm{d}} \dot{u}_i \mathrm{d}\Omega, \tag{3}$$

$$Q_{\bar{\mathrm{T}}} = -\int_{S} \bar{T}_i \mathrm{d}S, \tag{4}$$

is

$$L = \frac{1}{2}\int_{\Omega} \rho \dot{u}_i^2 \mathrm{d}\Omega + \int_{\Omega} m\boldsymbol{\sigma}_{ij} : \boldsymbol{\varepsilon}_{ij} \mathrm{d}\Omega - \int_{\Omega} f_i u_i \mathrm{d}\Omega, \tag{5}$$

where ρ is the density; μ_{d} is the damping coefficient, referring to Section 9.1.5 of Li et al. (2018); $\bar{T}_i$ is the surface force on the boundary; m is the mass of the block element; $\boldsymbol{\sigma}_{ij}$ and $\boldsymbol{\varepsilon}_{ij}$ are Cauchy's stress tensor and strain tensor, respectively (calculated using local coordinate system to avoid false strain caused by rigid body rotation); f_i is the body force, such as gravity and the inertia force.

In the CDEM framework, the whole domain is discretized by block and interface elements, and each interface element connects two adjacent block elements. Therefore, the internal fracture of the model can be described by block and interface elements. The interface elements are represented by a series of springs (one normal spring and two tangential springs), the breakages of which indicate the cracking processes. If all the springs at the interface break, the potential crack channel (black dashed line) is activated (black solid line), as shown in Fig. 1. If there are joints and other initial cracks in the domain, no springs are embedded in those positions.

Correspondingly, for these block and interface elements, different material laws are considered. Since rock is considered to be a quasi-brittle material, the block element is usually described by linear elasticity, and the interface element is described by the brittle Mohr–Coulomb (MC) model. In each iteration step, the block and interface elements are calculated in increments.

- For block element (linear elasticity),

$$\begin{cases} \Delta\boldsymbol{\sigma}_{ij} = 2G\Delta\boldsymbol{\varepsilon}_{ij} + \left(K - \frac{2}{3}G\right)\Delta\theta\delta_{ij} \\ \boldsymbol{\sigma}_{ij}(t_1) = \Delta\boldsymbol{\sigma}_{ij} + \boldsymbol{\sigma}_{ij}(t_0) \end{cases}, \tag{6}$$

where $\boldsymbol{\sigma}_{ij}$ and $\Delta\boldsymbol{\sigma}_{ij}$ are the total and incremental Cauchy's stress tensors, respectively; $\Delta\boldsymbol{\varepsilon}_{ij}$ is the incremental strain tensor; $\Delta\theta$ is the incremental bulk strain; K is the bulk modulus; G is the shear modulus; δ_{ij} is the Kronecker delta; t_1 is the next timestep; t_0 is the current timestep.

- For the interface element (brittle MC),

$$\begin{cases} F_{\mathrm{n}}(t_1) = F_{\mathrm{n}}(t_0) - k_{\mathrm{n}} \cdot A_{\mathrm{c}} \cdot \Delta du_{\mathrm{n}} \\ F_{\mathrm{s}}(t_1) = F_{\mathrm{n}}(t_0) - k_{\mathrm{s}} \cdot A_{\mathrm{c}} \cdot \Delta du_{\mathrm{s}} \end{cases}, \tag{7}$$

where $F_{\mathrm{n}}, F_{\mathrm{s}}$ are the normal and tangential contact forces; $k_{\mathrm{n}}, k_{\mathrm{s}}$ are the normal and tangential contact spring stiffnesses; A_{c} is the area of the interface element; Δdu_{n} and Δdu_{s} are the normal and tangential relative displacement increments, respectively.

2.2 Bar explosion model

Compared with the solid explosive source model in the finite element method, the bar explosion model employs 1D bar elements that are inserted into the solid block elements, as shown in Fig. 2, and directly transmits the detonation pressure to the nodes of the block elements that it penetrates. On the one hand, this approach avoids the distortion caused by the excessive expansion and deformation of traditional solid explosive elements; on the other hand, the grid in the area near the blasthole does not need to

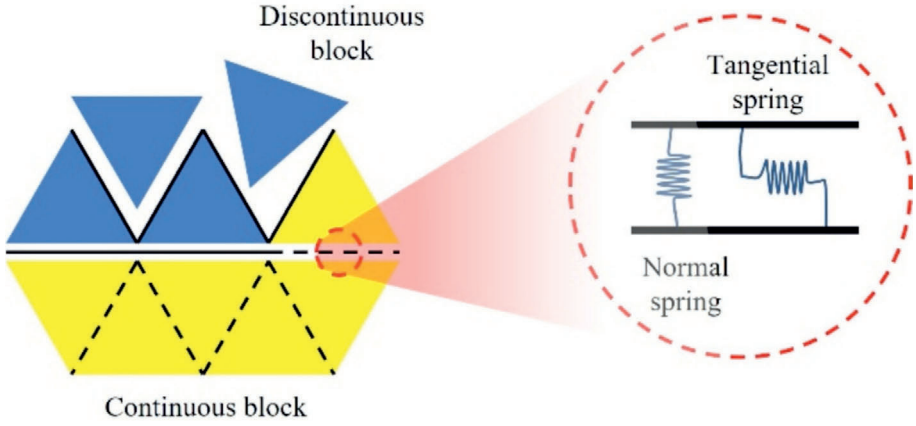

Fig. 1. Block and interface elements used in the CDEM.

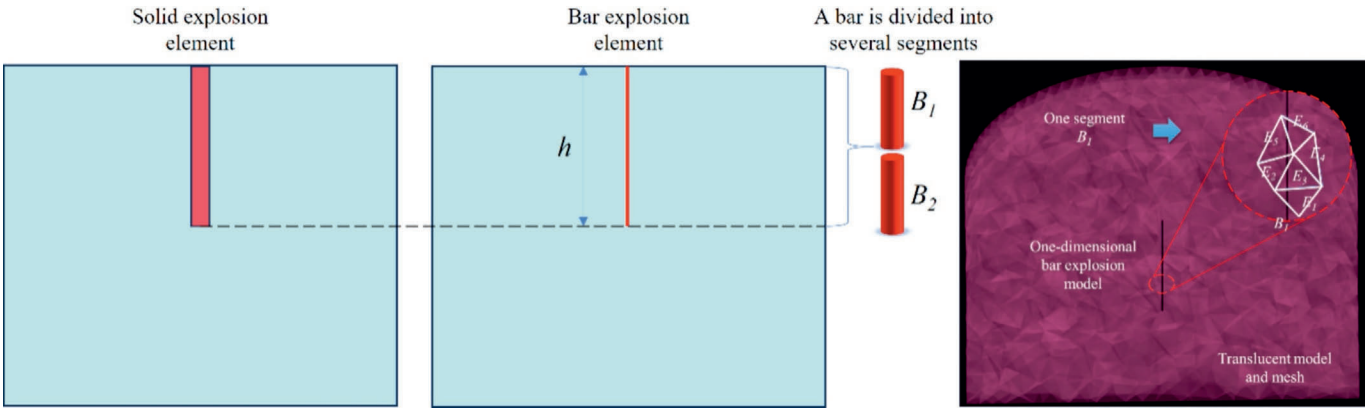

Fig. 2. Schematic diagram of the 1D bar explosion model.

be divided into particularly small grids to ensure that the solid explosive element and the nearby element grid are co-nodes, as shown in Fig. 3. Therefore, for large-scale 3D blasting numerical calculations, especially for multiple blasting holes, the number of elements required is greatly reduced when the bar explosion model is used.

The bar explosion model is numerically characterized by a 1D linear rod, which is equivalent to a cylindrical slender cartridge. In fact, once the length of a cylindrical charge is determined, a bar explosive element with equal length h can be established; the segmentation process simply requires that the length of each segment does not exceed the length of the solid element through which the bar penetrates. Thus, the initial volume V_0 can be calculated as follows. For clarity, the following explanation is provided using the subdivision of a segment as an example.

$$V_0 = \pi r_0^2 h, \tag{8}$$

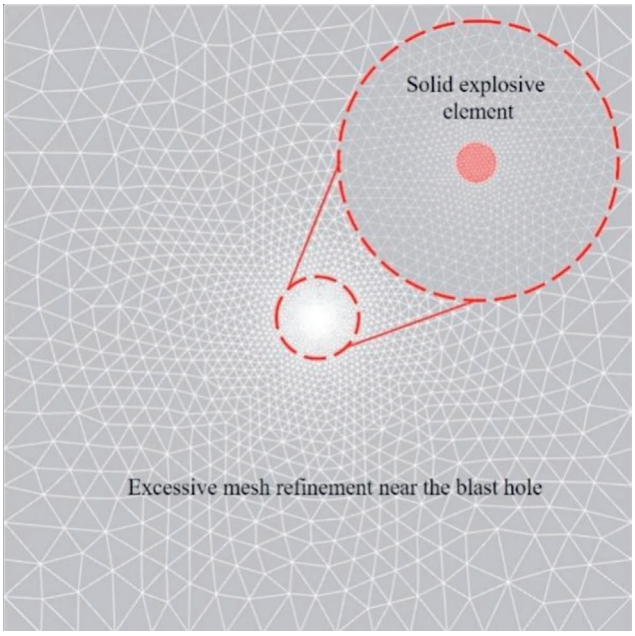

Fig. 3. Excessive mesh refinement near the blasthole.

where V_0 is the initial volume, r_0 is the initial radius of the explosive element, and h is the length of the explosive element. Because the element runs through adjacent block elements, its volume at the current moment V is given as follows:

$$V = V_0(1 + \theta_e), \tag{9}$$

where θ_e is the average volumetric strain of the explosive element, which can be obtained from the adjacent block elements through which it penetrates. Thus far, we have obtained the expanded volume of the explosive at a certain moment, which can be substituted into the Landau formula (Henrych, 1979) to calculate the detonation pressure of the explosive as follows (the bar explosion model can be adapted to other explosion models, and it is sufficient to modify its detonation-pressure equation to align with the JWL model).

$$\begin{cases} PV^{\gamma_1} = P_0 V_0^{\gamma_1} & P \geqslant P_c \\ PV^{\gamma_2} = P_c V_c^{\gamma_2} & P < P_c \end{cases}, \tag{10}$$

where γ_1 and γ_2 are the first and second adiabatic indices, respectively, and $\gamma_1 = 3$ and $\gamma_2 = \frac{4}{3}$ according to Feng et al. (2014); P and V are the detonation pressure and volume of the charge pack at the current time, respectively; the subscripts 0 and c represent the initial time and high-pressure time, respectively. P_0, P_c can be calculated as follows:

$$\begin{cases} P_0 = \frac{\rho_w^2 D}{2(\gamma_1+1)} \\ P_c = P_0 \left\{ \frac{\gamma_2 - 1}{\gamma_1 - \gamma_2} \left[\frac{(\gamma_1 - 1) Q_w \rho_w}{P_0} - 1 \right] \right\}^{\frac{\gamma_1}{\gamma_1 - 1}} \end{cases}, \tag{11}$$

where ρ_w is the density of the charge, Q_w is the explosive heat of the explosive, and D is the detonation velocity.

The distance from the ignition point to the centre of the bar explosion element is assumed to be d (i.e., the detonation pressure transfer to adjacent solid elements initiates only after the explosive combustion process progresses to its halfway point). The set ignition time is denoted as t_{D_0}. The ignition time t_{D_1} of the bar explosion element is $t_{D_1} = \frac{d}{D} + t_{D_0}$. When time t is greater than t_1, the bar explo-

sive element begins to calculate the true detonation pressure P_r.

$$P_r = \xi f(P), \tag{12}$$

where ξ is the explosive energy release rate, which is calculated via Eq. (13). $f(P)$ is the Landau formula in Eq. (12).

$$\xi = \begin{cases} \min\left[\frac{(t-t_1)D}{h}, 1\right] & t > t_1 \\ 0 & t \leqslant t_1 \end{cases}. \tag{13}$$

2.3 Numerical calculation flow

When the bar explosion model is employed, the transfer of detonation pressure is a key component of the bar explosion model due to the noncoincident nodes between the bar elements and the surrounding solid block elements. We bind the bar explosive elements to the solid block elements they penetrate to establish a pressure–volume coupling relationship. This finding suggests that the detonation pressure of the bar model is distributed to the nodes of the solid block elements. Furthermore, the volumetric expansion of the solid elements is considered as the explosive expansion volume of the bar element at a certain moment, as shown in Fig. 2. Since a bar element (B_1) penetrates N solid elements ($E_1, \cdots, E_6$), the detonation pressure is shared among them. Moreover, as the explosive pressure attenuates with increasing distance, the actual detonation pressure on the penetrated element nodes must be calculated according to Eqs. (14) and (15). Finally, the actual detonation pressure is transformed into a nodal force applied to the element nodes, as shown in Eq. (16) (considering a tetrahedral element (C3D4) as an example).

$$\bar{P}_r = \frac{1}{N}\sum_{i=1}^{N} P_{r_i}, \tag{14}$$

$$\sigma_b = -\bar{P}_r\left(\frac{r_0}{L_c}\right)^a, \tag{15}$$

where $\bar{P}_r$ is the average detonation pressure (evenly distributed to four nodes); N is the total number of solid block elements penetrated by the bar explosive element; σ_b is the corrected detonation pressure at the element node; r_0 is the initial radius of the bar explosive element; L_c is the feature size of the element; and a is the attenuation coefficient, which can be obtained by systematically monitoring the peak detonation pressure through comparative analysis against the operational conditions of the solid explosion case. Through the comparison in Section 3.1, $a = 1.25$ is considered appropriate.

$$F_i^N = -\int_S \sigma_b n_i \mathrm{d}S \approx -\sigma_b \sum_{k=1}^{3}\left(n_i^k \frac{\Delta S^k}{3}\right), \tag{16}$$

where F_i^N is the nodal force in the ith direction on the Nth node of a solid block element; k is the serial number of the three faces associated with node N; n_i^k is the component of the element outside the normal vector of the k-th surface associated with node N in the i-direction; ΔS^k is the area of the kth surface.

Thus, we simplify the solid explosion source model into a 1D bar explosion model within the CDEM framework for calculation, as illustrated in Fig. 4.

3 Blasting verification

3.1 Blasting wave and damage characteristics

We have developed a 2D cut blasting model with a single hole. This case serves two purposes: to better illustrate the embedding of the bar explosion model within the elements and to verify its accuracy. The model is 4 m in length and 2 m in height, the diameter of the blasthole is 10 cm, and the depth is 0.5 m. The explosive is an emulsion that adopts a fully coupled charging structure, and its detonation parameters are shown in Table 1. The model is meshed using both quadrilateral and triangular elements. The rock part is meshed with triangular elements, whereas the explosive part is meshed with quadrilateral elements, resulting in a total of 7237 triangular elements and five quadrilateral elements (the element size is 0.1 m).

The mechanical parameters of the rock are shown in Table 2. Figure 5(a) shows the geometric information of the model, and Fig. 5(b) shows the computational mesh of the model. We set up three monitoring points to monitor the changes in the explosion stress wave with increasing distance. The left side of Fig. 5(b) represents the solid explosion case, and the right side represents the bar explosion case. To avoid errors caused by the differences in the meshes, both cases share the same mesh.

We plot the von Mises stress cloud diagrams of the two cases as shown in Fig. 6. Unlike a spherical charge explosion, which involves concentric circular diffusion, a columnar charge explosion first generates a strong detonation wave at the bottom of the explosive (the ignition point). The explosive stress wave then expands from the bottom to the top. After the entire charge detonates, it begins to propagate outwards. At $t = 0.25$ ms, the explosion stress wave is in the shape of a droplet, and the entire columnar charge detonates. By $t = 0.75$ ms, the wave has already spread outwards to the edge of the model in the shape of a semicircle, with a peak stress of 265.2 MPa. In terms of the characteristics of the explosive stress wave at each stage, the bar explosion model and the solid explosion model behave basically the same.

In addition, we plot the time-history curves of the explosion stress at the monitoring points for both cases to quantify and compare the results, as shown in Fig. 7. The curves of the two conditions are basically consistent. The rising and decaying trends of the explosion stress wave are similar, but there are errors in the peak explosion stress. At 2 m, the peak stress error is 3%; as the wave propagates outwards, the maximum peak error reaches 20%. This phe-

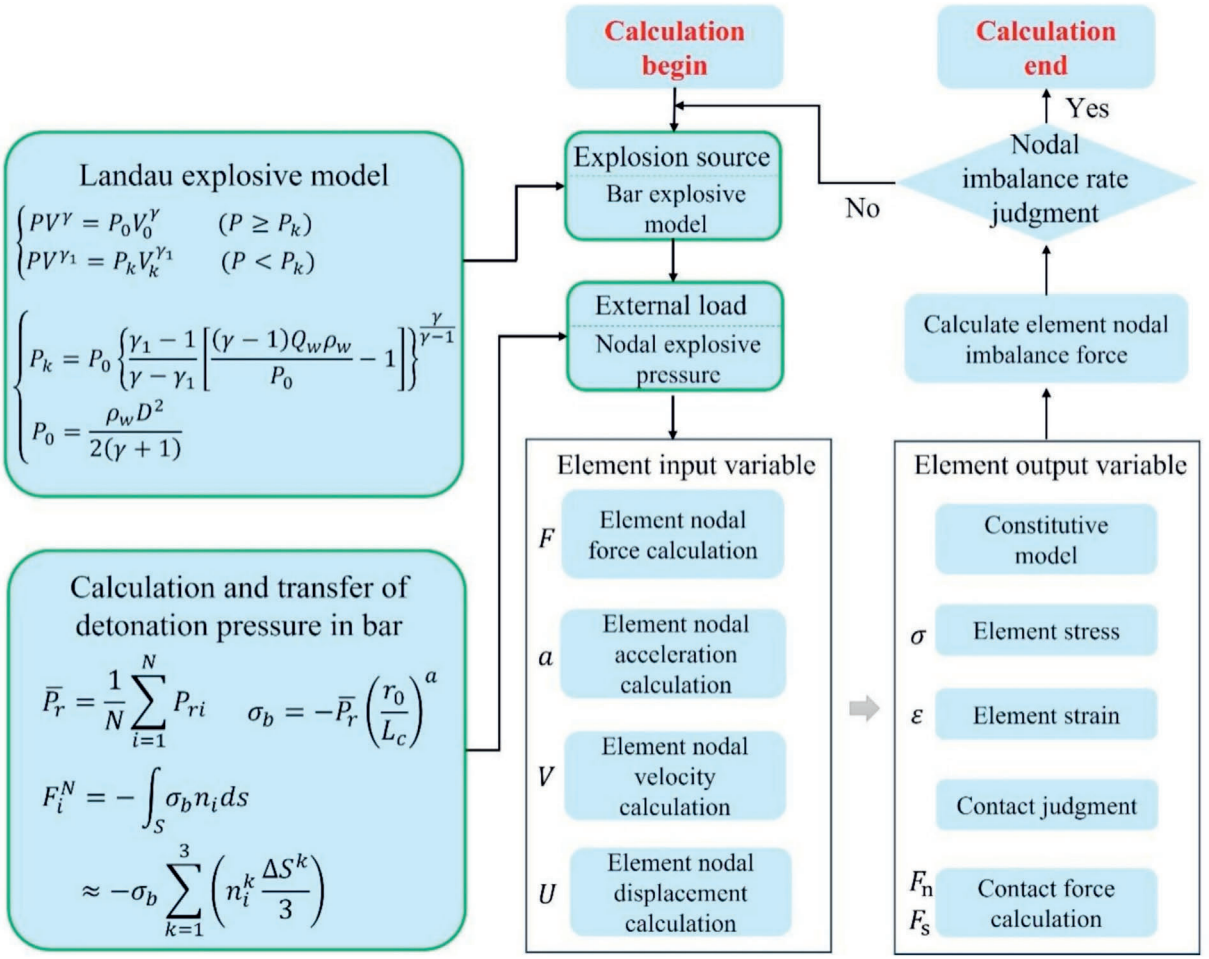

Fig. 4. Block and interface elements used in the CDEM.

nomenon may arise due to the slight delay in the blasting of each segment of the bar explosion model and the phase difference caused by the stress wave superposition. Overall, the explosion stress wave curves exhibit the same trend, and the peak errors are acceptable.

Table 1
Detonation parameters of emulsion explosive (Feng et al., 2022).

Material properties	Value
Charge density ρ (kg/m^3)	1150
Detonation velocity D (m/s)	5000
Explosive heat Q_w (J/kg)	3.1×10^6
Phase 1 adiabatic index γ_1	3.0
Phase 2 adiabatic index γ_2	1.33
Detonation pressure P (Pa)	7×10^9

Table 2
Rock mechanical parameters (Feng et al., 2022).

Material properties	Value
Density ρ (kg/m^3)	2500
Modulus of elasticity E (GPa)	10
Poisson's ratio μ	0.25
Cohesive force c_0 (MPa)	10.0
Tensile strength f_t (MPa)	4.00
Angle of internal friction ϕ (°)	10

The damage cloud diagrams for the two cases are shown in Fig. 8. Here, 0 indicates no damage, and 1 indicates total damage. Like the various stages of the explosion stress wave, the damage process can be divided into four stages. At $t = 0.15$ ms, the damage first appears at the bottom of the blasthole. At $t = 0.20$ ms, the damage is teardrop shaped, matching the explosion stress wave. At $t = 0.8$ ms, the damage is butterfly shaped, extending to the lower left and right areas of the model. At $t = 3$ ms, the detonation ends, and the damage stabilizes, forming a swallow-shaped area. In the centre of the "swallow's tail", due to the strong constraint at the bottom, some stress waves are reflected, resulting in triangular damage. The damage distribution characteristics of the two cases are highly consistent for each stage. Notably, owing to the establishment of the solid explosive element, there are undamaged explosive elements in the centre of the solid explosion case, and a blank area forms after the completion of the detonation at $t = 3$ ms. Correspondingly, there are no solid explosive elements in the bar explosion case; thus, the above situation does not exist.

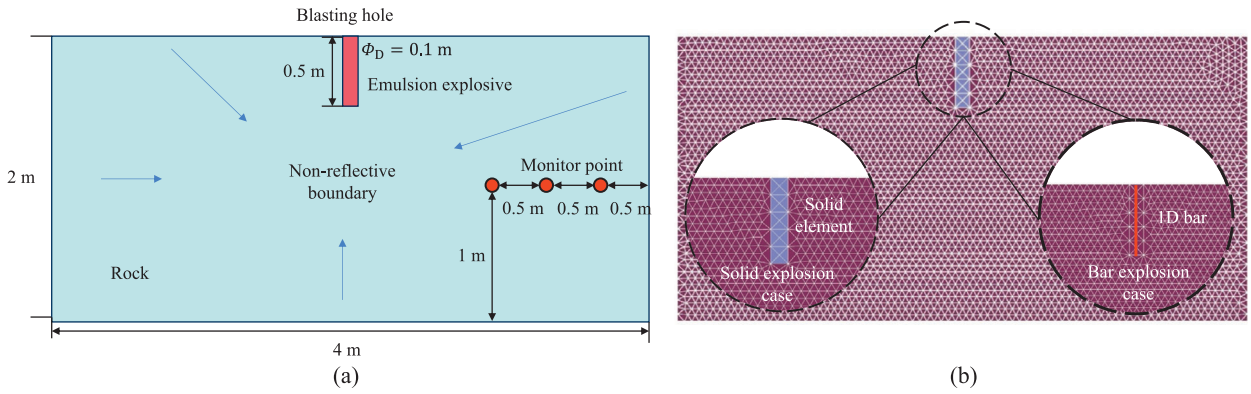

Fig. 5. Model of solid explosion case and bar explosion case. (a) Modeling geometric information, and (b) comparison of numerical grids of two cases.

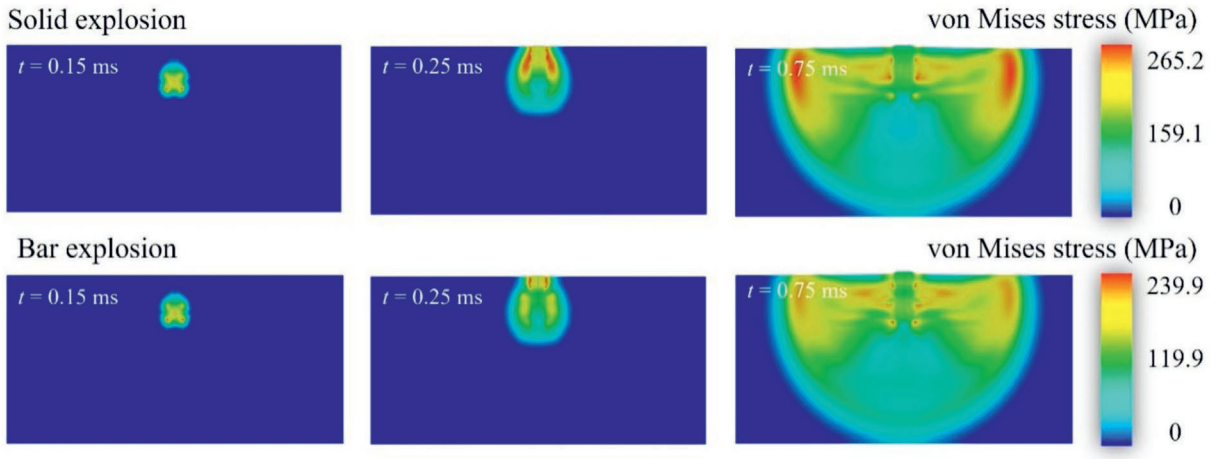

Fig. 6. Comparison of the explosion stress wave characteristics in the two cases.

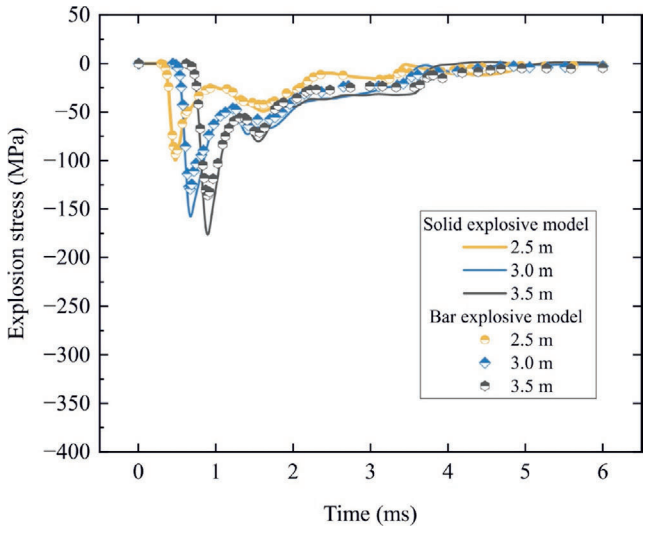

Fig. 7. Explosive stress time-history curves of the two cases.

3.2 Computational efficiency

We numerically replicate the case of multihole blasting in a tunnel. The geometric dimensions and mechanical parameters of the model match those of the reference (Xu et al., 2025). We set up two cases—a solid explosion and a bar explosion—to compare the calculation efficiencies. The mesh is divided by a tetrahedron, as shown in Fig. 9, where Fig. 9(b) is the solid explosion case, and Fig. 9(c) is the bar explosion case.

For the boundary area and thickness direction of the model, we set the two cases to be consistent to reduce the influence of these factors on the number of elements. The solid explosion case is obviously encrypted in the blasthole area due to the difference between the hole size and the overall size of the model, and a total of 338 790 tetrahedral elements (with an element size of 0.03–0.20 m) are divided (we divide only one element in the blasthole area to minimize the number of elements). However, the bar explosion case does not need to be encrypted, and only 50 820 tetrahedral elements (with an element size of 0.1–0.2 m) are divided.

The damage nephograms for the two cases are shown in Fig. 10. The fracture processes of both cases are consistent with the reference description. In addition, we place monitoring points at every 30° to measure.

The damage and plot the damaged area as shown in Fig. 11. The results of the two cases are basically the same, and the errors are very small.

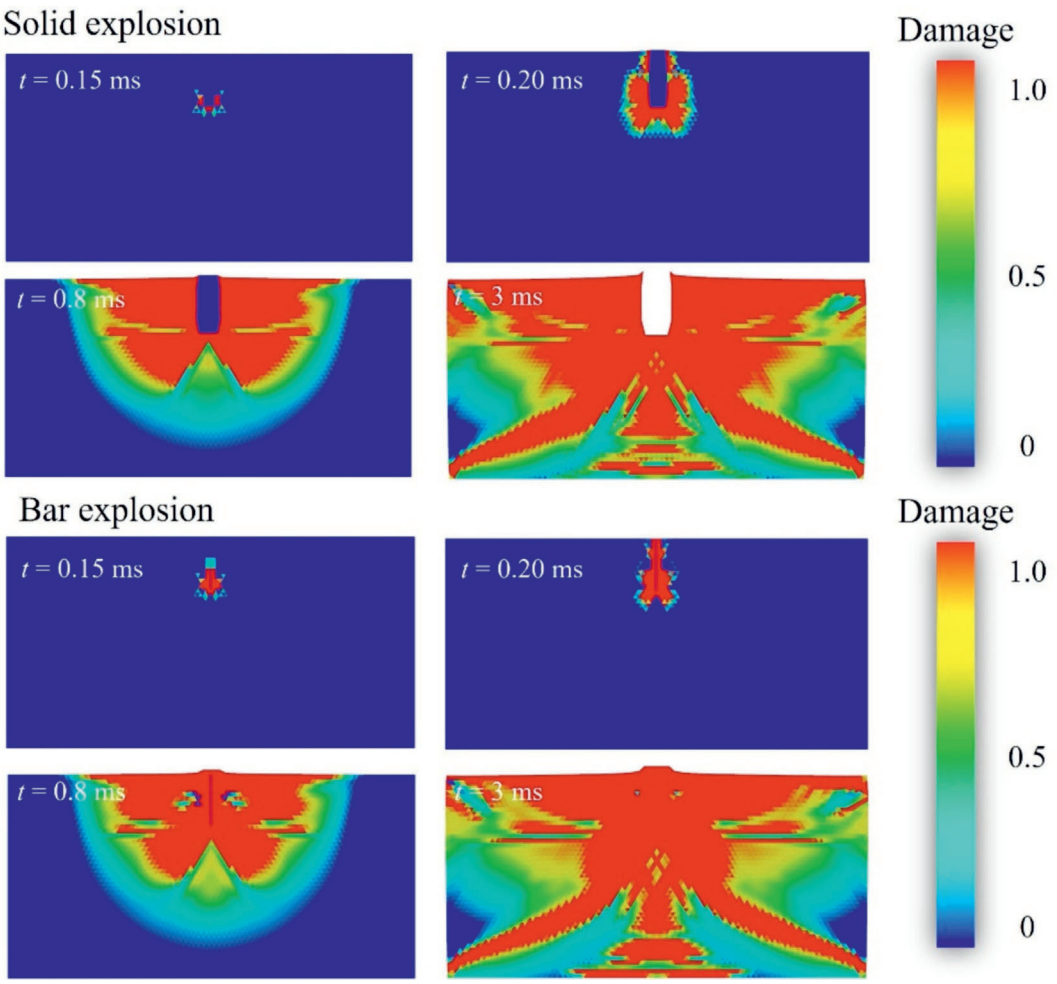

Fig. 8. Damage nephogram of the two cases.

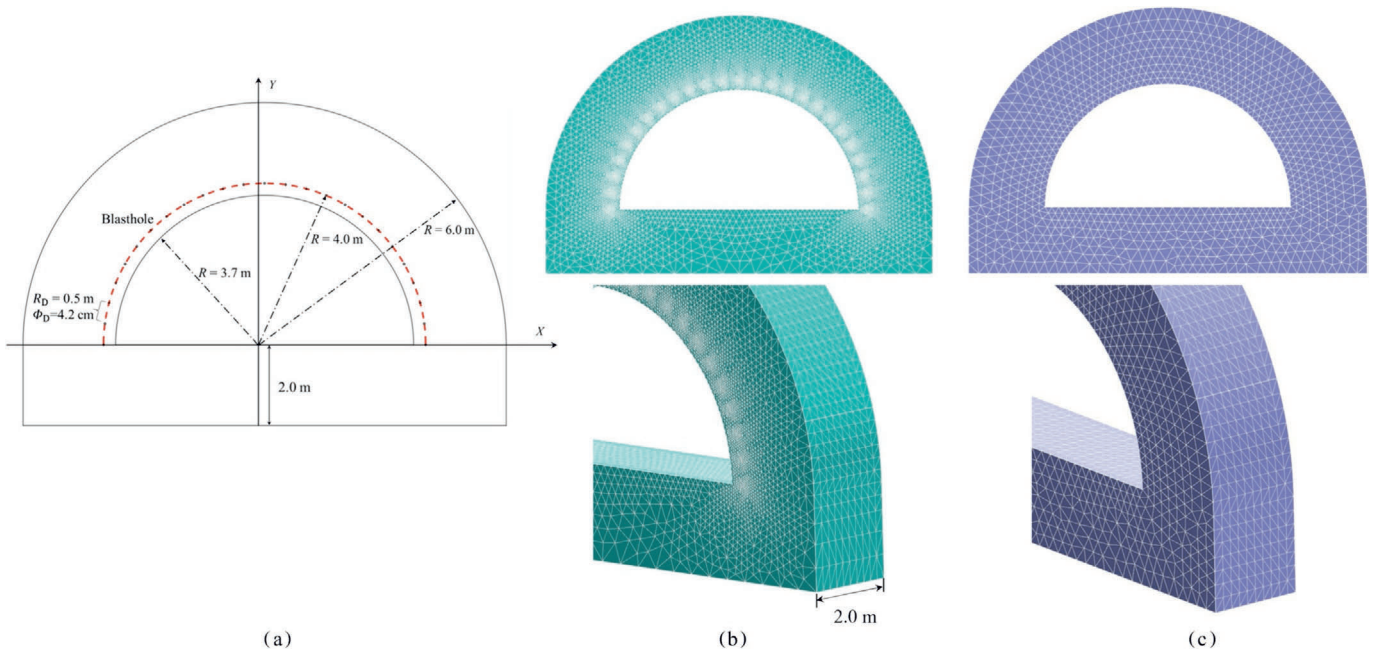

Fig. 9. Geometric information of the model and computational grid. (a) Model geometry data (redrawn from Xu et al., 2025), (b) solid explosion case computational grid, and (c) bar explosion case computational grid.

In terms of computational efficiency, a personal computer with an Intel Core i9-13900 K processor, 196 GB of RAM, and NVIDIA RTX4090 is used to obtain the numerical results. This computer takes 999 279 ms for the solid explosion case but only 132 497 ms for the bar explosion case, which improves the calculation efficiency by 7 times. This result arises mainly because there is no need to refine the elements near the blasthole for the bar explosion case, and the total number of elements is only 15% of that in the solid explosion case.

4 Engineering application

Cut blasting is a common method applied in excavation projects designed to fracture a rock mass as required without causing undue damage to the tunnel walls or surrounding rock. Thus, accurately controlling the blasting effects and the range of damage is central to the study of cut blasting. Based on the engineering demands for foundation pit blasting excavation at Ramp 2 in the P-junction of the Qingtian–Wencheng Expressway, we conduct a numerical simulation study on cut blasting with the support of the China Railway 16th Bureau Group.

4.1 Model

Based on the engineering background, a 3D numerical model is established, as shown in Fig. 12(a). The model is 1.8 m in diameter and 2.0 m in height. There is a prefabricated 40 mm empty hole at the centre of the model, with the remaining blastholes arranged via the bar explosion model. A high-damping ring is set around the model as shown in the red area in Fig. 12(a), to absorb the compressive stress waves at the edges and simulate the no-reflection boundary conditions. In addition, monitoring points are arranged at the top of the model to monitor the vertical displacement of the model (the red points in Fig. 12(a)). These points are located 0.050, 0.015, 0.300, 0.500, and 0.800 m away from the centre of the model, respectively, to monitor the ejection height at the top to evaluate the blasting effect.

The model is discretized with a nonuniform tetrahedral mesh featuring a mesh size of 0.012 m in the central empty whole region and 0.1 m at the periphery, with a gradual transition in mesh size from the centre to the edge. The high-damping region is meshed uniformly at 0.15 m to reduce the computational load. The model consists of 31 825 block elements and 336 126 interface elements. The block element adopts a linear model, the interface element adopts a fracture energy model, and its mechanical parameters are obtained from an engineering geological investigation report, as shown in Table 3. The bar element adopts the Landau model, and the explosive is an RDX explosive. The detonation parameters are shown in Table 4.

The plane layout and charging structure of the blastholes are shown in Fig. 12(b) and (c). The basic whole layout of the three cases is shown in Fig. 13. Three cases share identical expansion hole layouts (#2 and #3), with the primary distinction residing in their cut hole configurations. Both Cases A and B employ one-stage cut blastholes (#1), whereas Case C uses a two-stage cut configuration (#1). Delayed blasting is adopted to reduce the possibility of flying stones. In Fig. 12(c), the blue section represents the hole blockage section, and the red represents the charging section. According to the initiation sequence and charge structure, three blasting cases are designed as shown in Table 5. The initiation points of the three cases are all at the bottom of the cylindrical charge and detonate from bottom to top.

4.2 Numerical results

4.2.1 Displacement comparison

According to the blasting ignition time of each stage of the three cases, the vertical displacement cloud diagrams of the three cases are drawn as shown in Figs. 14–16. The fig-

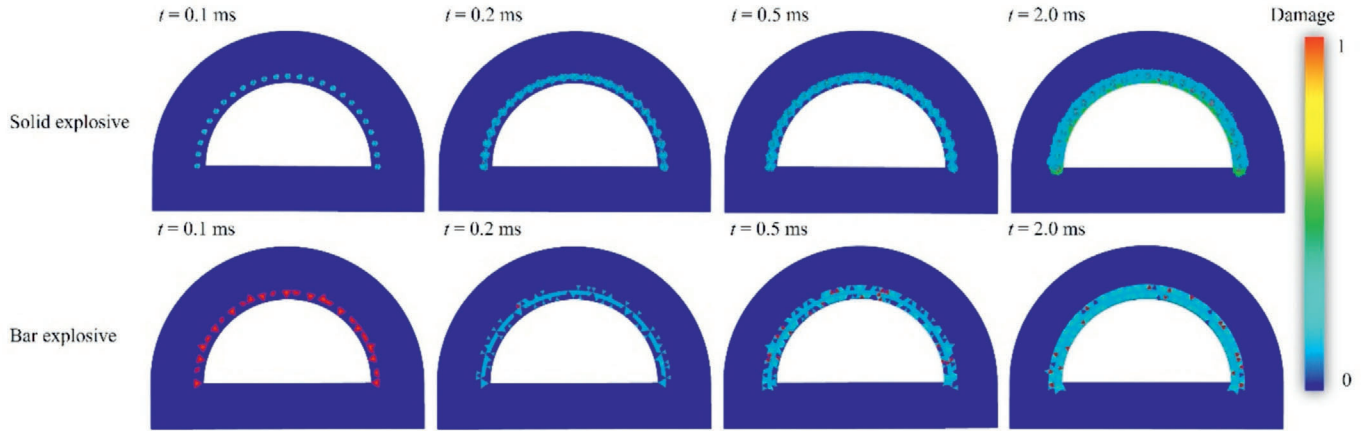

Fig. 10. Fracture process of two cases.

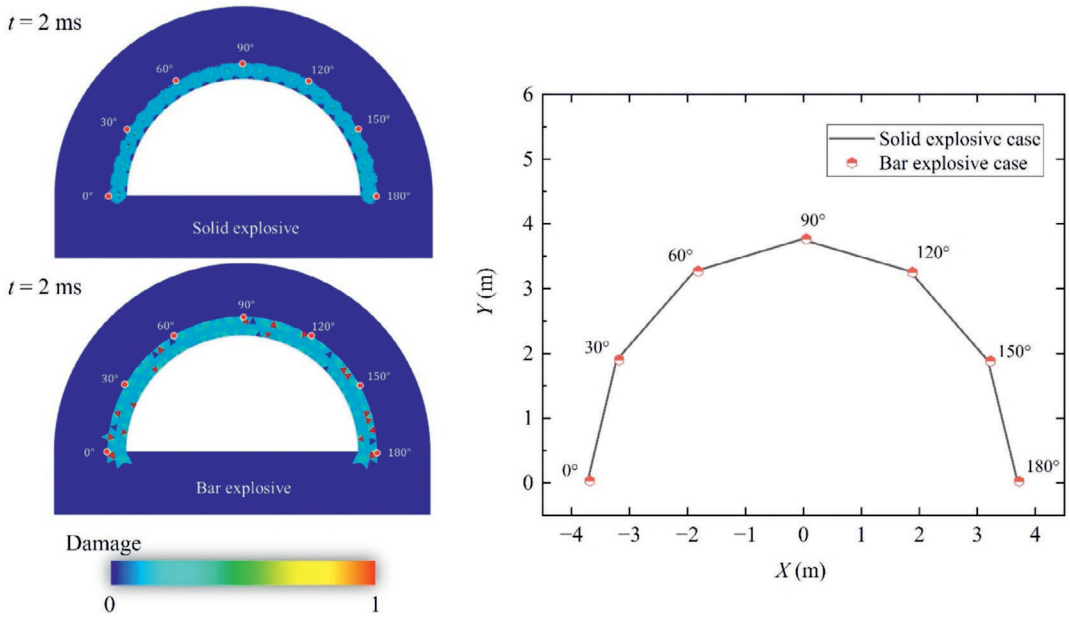

Fig. 11. Comparison of damage zone under two cases.

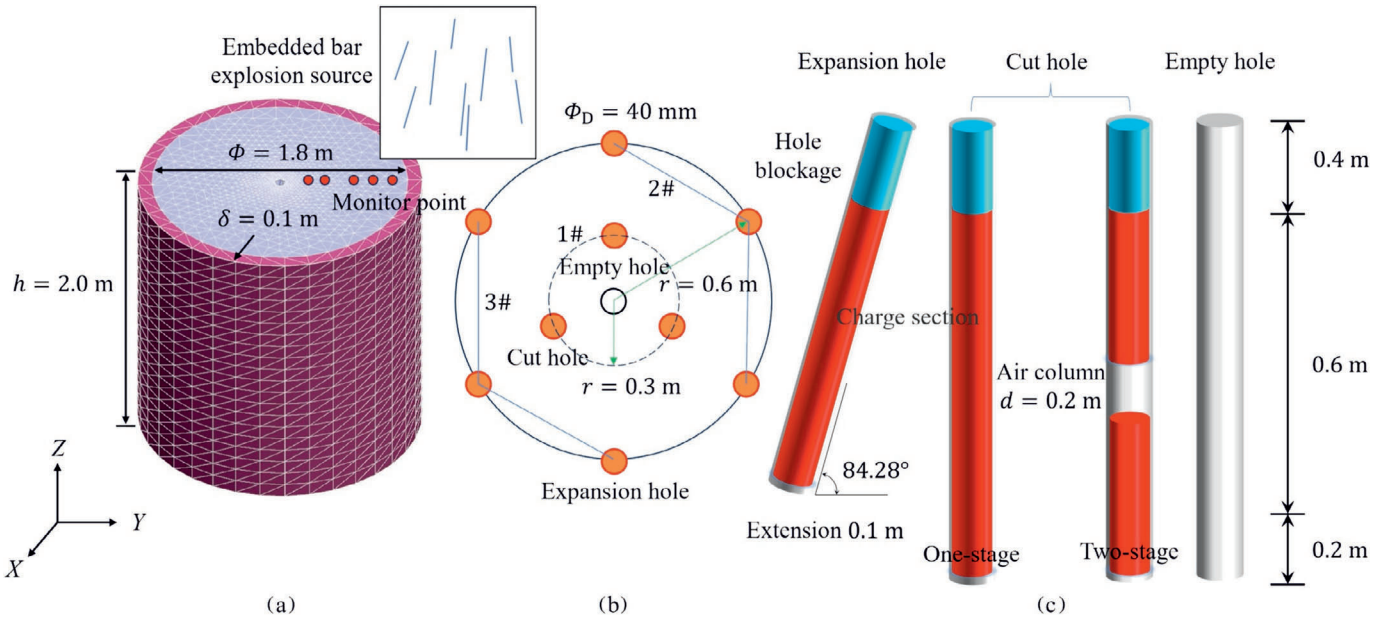

Fig. 12. Numerical model and hole layout. (a) Numerical model, (b) hole layout, and (c) charge structure.

ures show that the blasting results of the three cases are quite different, with a maximum vertical displacement difference of 4.6 times.

Case A is a one-stage cut blasting, in which all the blastholes are detonated simultaneously. The entire blasting process can be divided into three stages as shown in Fig. 14, including the detonation phase (0 – 2 ms), the damage phase (2 – 8 ms), and the ejection phase from 8ms to 0.05s. At 0ms, all blastholes are ignited and detonated at the same time. At 1.3 ms, sporadic debris is observed entering the central empty hole, with the model's top not yet exhibiting significant cracking. By 2 ms, the U_Z (displacement along the Z direction) cloud diagram indicates noticeable displacement characterized by a funnel shape with a larger centre and smaller edges. At this moment, the displacement of the crushing zone at the top of the model is approximately circular, but surface cracking is not significant. Overall, the amount of debris is large. To prevent differences in the grid from influencing the fragment size, the same grid is used in three cases, with only the blasthole layout being different. There are three radial main cracks (black lines) and numerous circumferential cracks

Table 3
Mechanical parameters of the pile blasting excavation model.

Material properties	Value
Density ρ (kg/m^3)	2681
Modulus of elasticity E (GPa)	99.3
Poisson's ratio μ	0.28
Cohesive force c_0 (MPa)	20
Tensile strength f_t (MPa)	8.11
Angle of internal friction ϕ (°)	35
Shear dilatancy angle θ_S (°)	15
Tensile fracture energy E_T (Pa · m)	70
Shear fracture energy E_S (Pa · m)	700

Table 4
Detonation parameters of emulsion explosive (Feng et al., 2022).

Material properties	Value
Charge density ρ (kg/m^3)	1820
Detonation velocity D (m/s)	8350
Explosive heat Q_w (J/kg)	5.4×10^6
Phase 1 adiabatic index γ_1	3.0
Phase 2 adiabatic index γ_2	1.33
Detonation pressure P (Pa)	32×10^9

(white lines). In terms of displacement after blasting, there is a significant time lag, with noticeable changes in displacement occurring approximately 1 ms after the detonation period ends. At 3 ms, the blasting funnel has a prototype, and the cracks at the top of the model have widened and increased in visibility. Then, at 8 ms, the ejection phase begins, by which time the blasting funnel forms and is essentially separated from the bedrock. The vertical displacement in the central empty whole area is the greatest at this moment. As time progresses, the area with displacement exceeding 0.1 m gradually spreads from the central area to the surroundings and is approximately circular until it eventually covers the entire blasting funnel. At 0.05 s, the ejection reaches its maximum height, with the maximum vertical displacement being 0.533 m.

Case B is a single-stage cut blasting process, which differs from Case A in that the inner circle of the blast holes is detonated first to create a free face for the outer circle of the blastholes, followed by the symmetric detonation of the outer circle blastholes with a blasting time interval of 0.01 s. According to the initiation time of the blastholes, we draw a Z-direction displacement cloud map for Case B as shown in Fig. 15. At 2 ms, obvious displacement may be observed from the profile of the Z displacement cloud map, and there is a new crushing area at the top of the model. However, the crushing degree is very low. The crush diameter is smaller than that in Case A, with the displacement mainly being concentrated in the right area of the empty hole. At 6 ms, the blasting funnel of the inner circular blastholes is essentially formed, and it begins to enter the ejection phase. At this moment, the diameter and crack degree of the top crushing zone no longer

Table 5
Three blasting schemes.

Case number	Cutting method	Initiation sequence
Case A	One-stage cut	#1, #2, #3 simultaneously detonates
Case B	One-stage cut	#1→#2→#3 sequentially detonates
Case C	Two-stage cut	#1→#2→#3 sequentially detonates

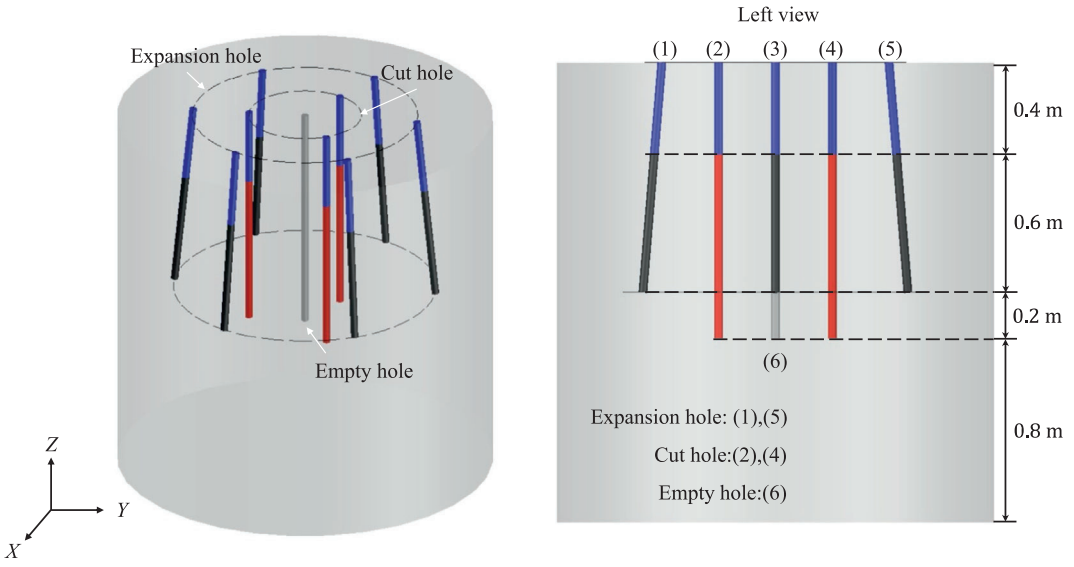

Fig. 13. Blasthole layout.

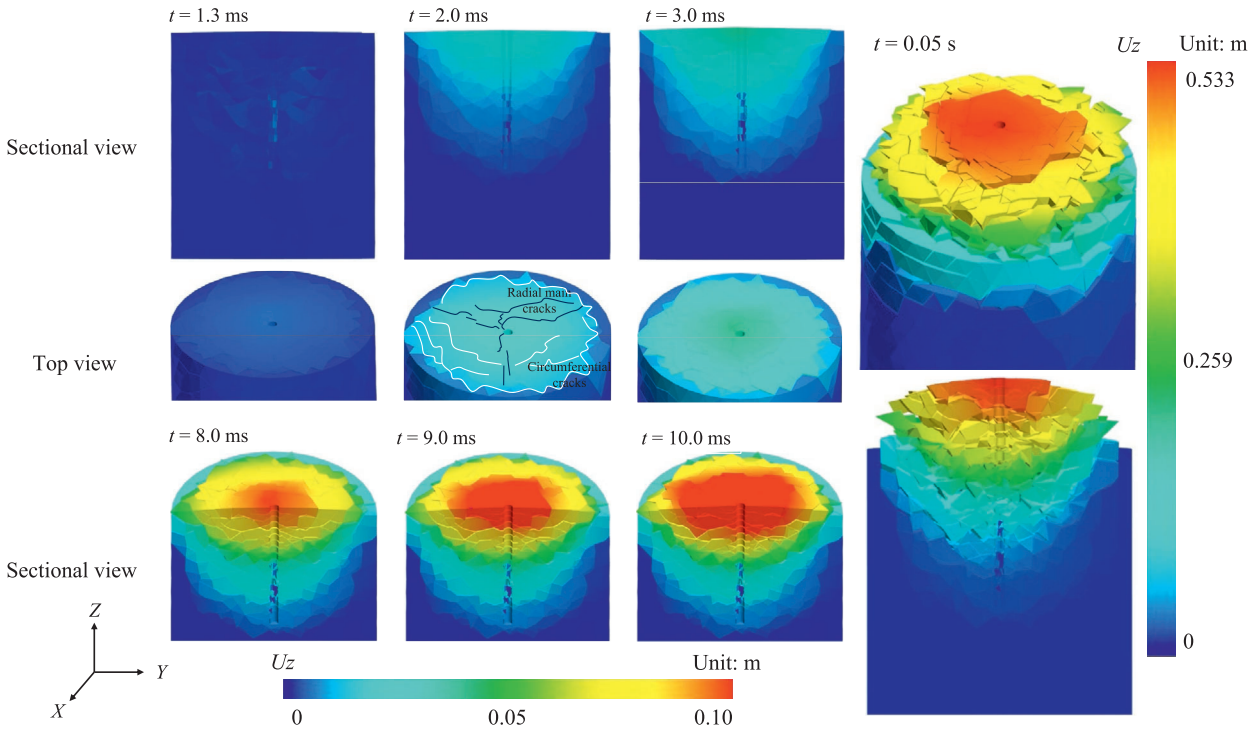

Fig. 14. Case A displacement in the Z direction.

change. At 0.023 s, with the detonation of the blastholes on the right side of the outer circle, an additional displacement is again generated in the lower right area of the central empty hole. We select this area for local enlargement and draw a Y direction displacement cloud map with a vertical displacement that increases by approximately 0.01 m and collapses inwards by 0.007 m. In addition, the diameter of the crushing zone at the top of the model further expands, and the right area of the model radially increases by approximately 0.12 m. At 0.032 s, when the left sides of the outer circles of the blastholes are detonated, the left rock collapses inward by approximately 0.004 m. At 0.05 s, the ejection reaches its maximum height, with the maximum vertical displacement being 0.177 m, which is significantly lower than that in Case A.

Case C is a two-stage cut blasting process, and its initiation sequence is the same as that of Case B. However, the inner circular blasthole is changed to two-stage blasting as shown in Fig. 12(c). At 0 ms, the upper blastholes in the inner circle are first detonated. At 2 ms, a significant displacement is observed in the vertical displacement cloud map, forming as a prototype of the blasting funnel. From the top view, the displacement is triangular and basically distributed at the blastholes. At 8 ms, the inner circle in the crushing zone exhibits a more obvious triangular feature. At this time, the blasting funnel of the first blasting is essentially formed; it splits with the bedrock and is thrown upward. At 0.01 s, the lower blastholes in the inner circle are detonated, and local cracking occurs. However, the vertical displacement is not obvious. After the outer circular blast holes are detonated at 0.02 and 0.03 s, the bottom area of the central empty hole begins to show obvious vertical displacement at approximately 0.1 m. At 0.05 s, the ejection reaches its maximum height, and the maximum vertical displacement is 0.829 m. Compared with those of Cases A and B, the central area of Case C is the most broken, and the overall ejection displacement is the largest.

Additionally, the Z-direction displacement time-history curves for the three cases are shown in Figs. 17–19. In general, the vertical displacements at the monitoring points for all three cases increase with time, but there are significant differences locally. As shown in Fig. 17, the displacement time curves of the monitoring points at 0.05, 0.15, and 0.30 m in Case A basically overlap, and the maximum vertical displacement is 0.533 m. The vertical displacement begins to decrease sharply at 0.50 m outside the central hole, and at 0.08m, the peak vertical displacement is only 0.041 m. At $t = 0.02$ s, only Case A monitors the vertical displacement at 0.08 m, indicating that the detonation intensity of a single initiation is greater and that the damage range of the model is larger.

As shown in Fig. 18, Case B's vertical displacements at the monitoring points of 0.05, 0.15, 0.30, and 0.50 m are essentially consistent, and the peak value is relatively small at 0.101 m; even at 0.80 m, the peak displacement is only 0.044 m. This finding indicates that the damage range at the top of the model is small and that the degree of damage is low, as shown in Fig. 15. The blasting scheme in Case B effectively limits the flying height of the blasting fragments.

As shown in Fig. 19, the displacement time-history curves at the two monitoring points of 0.05 and 0.15 m in Case C are basically the same, with a displacement peak

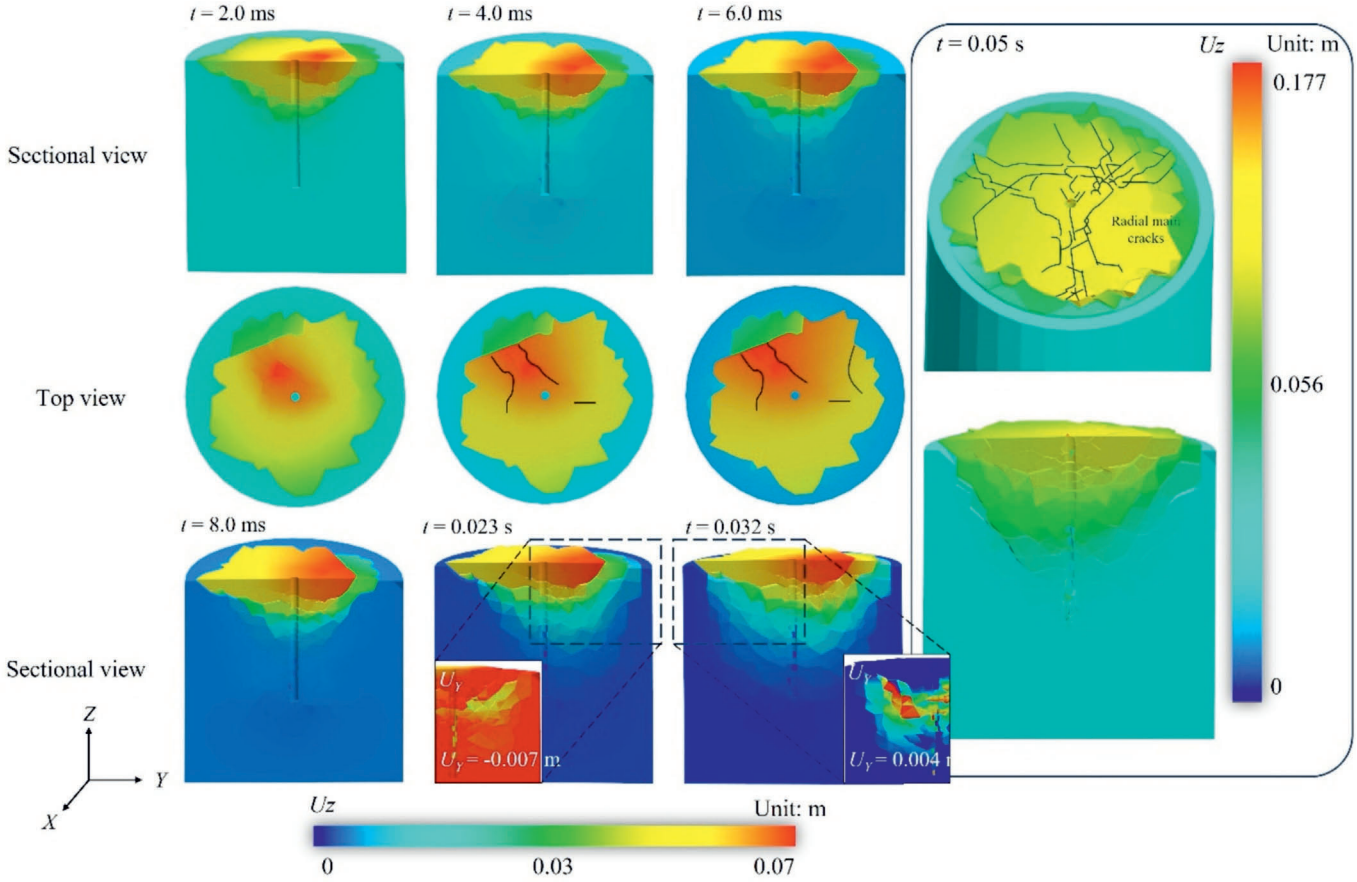

Fig. 15. Case B displacement in the Z direction.

value of 0.77 m. The vertical displacement begins to decline linearly beyond a distance to the centre hole of 0.15 m. The displacement characteristics indicate that the top area of the Case C model is generally more uniformly broken, and the problem of flying stones after blasting is the most serious.

Three moments, 0.01, 0.03, and 0.05 s, are selected to plot the displacement variations for different centre distances under three different conditions, as shown in the miniature plots in Figs. 17–19. There are significant differences among the three conditions. In Case A, the vertical displacement begins to noticeably decrease at 0.5 m. Case B has a decreasing distance similar to that in Case A, but its peak vertical displacement is only 20% of that in Case A. Case C exhibites a clear decrease in the vertical displacement at 0.15 m, with an overall decline that is approximately linear, indicating an overfragmentation issue in the crush zone of the blasting process. Therefore, in terms of the flying stone problem in pile foundation pit blasting excavation, Case B is the optimal blasting scheme.

4.2.2 Damage distribution

The blasting damage characteristics of the three cases are similar; thus, we choose the most complex two-stage cut blasting case to analyze the damage situation. Based on the timing of the four detonations, von Mises stress and damage diagrams are plotted as shown in Fig. 20. When $t = 0.04$ ms, the upper blastholes of the inner circle explode, resulting in a strong blasting stress visible in the centre of the model. At this moment, the stress wave is approximately dumbbell-shaped and diffuses from the centre of the model to its periphery. At $t = 0.01$ s, the lower blastholes of the inner circle are detonated. The blasting crater from the first detonation has essentially developed and detached from the bedrock. Thus, the blasting stress wave accumulates in the lower middle part of the model and shows a downwards expansion trend, which is the key factor contributing to the increased footage during two-stage cut blasting. When $t = 0.02$ s, the holes on the right side of the outer circle explode, and the detonation stress tends to transfer from right to left. When $t = 0.03$ s, the hole on the left side of the outer circle explodes, and the detonation stress wave propagates from left to right. The outer circular hole contributes little to the crushing area at the top of the model, but has a greater effect on expanding the damage range in the middle.

The lower part of Fig. 20 shows the damage diagram, where 0 represents no damage, 1 represents tensile damage, and 2 represents shear damage. At the beginning of each stage of blasting, the shear damage is mainly in the area

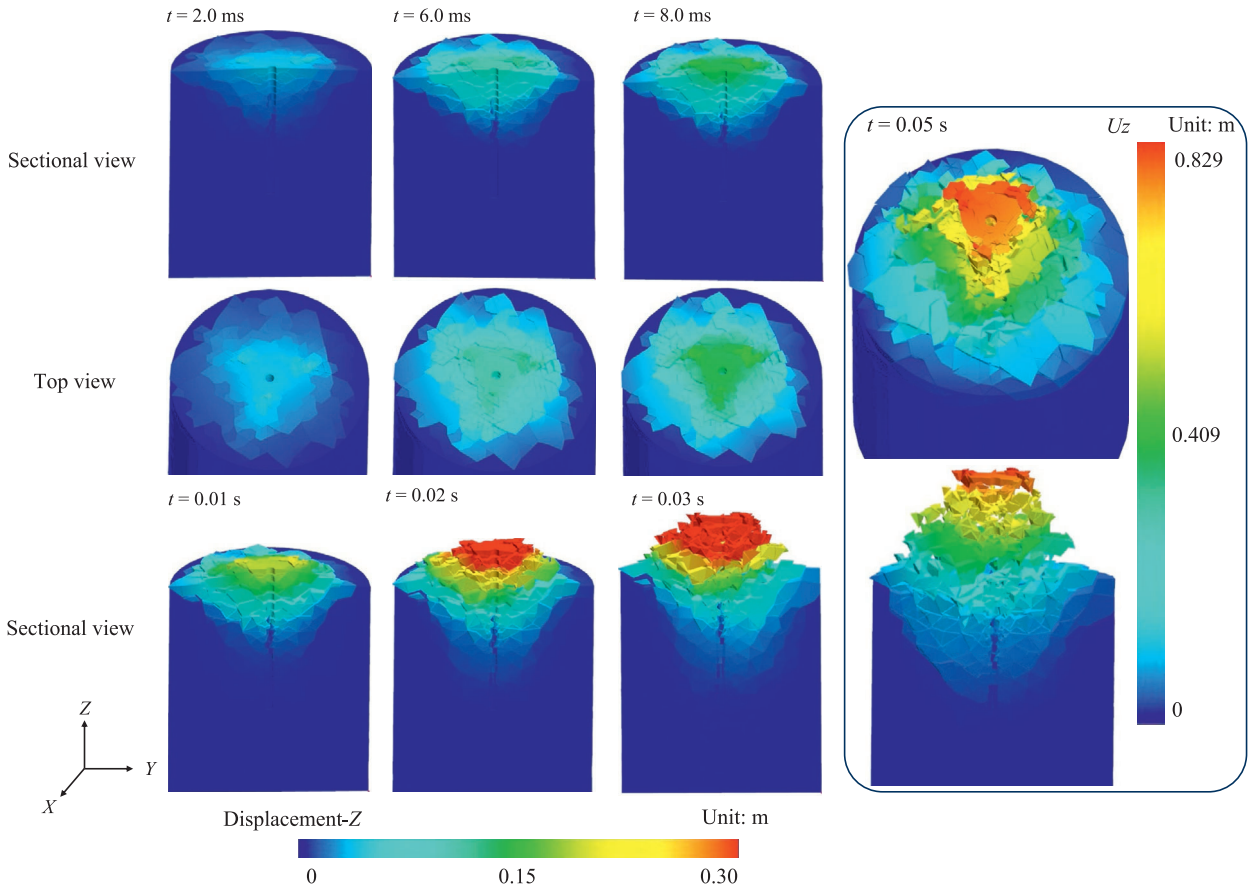

Fig. 16. Case C displacement in the Z direction.

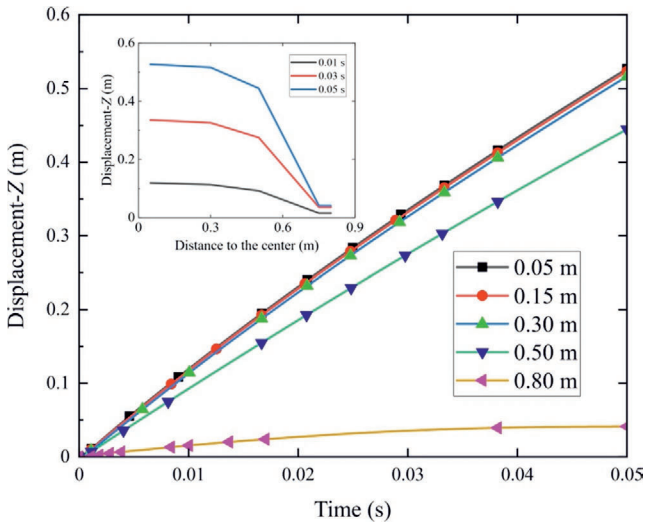

Fig. 17. Case A's Z-direction displacement time-history curve.

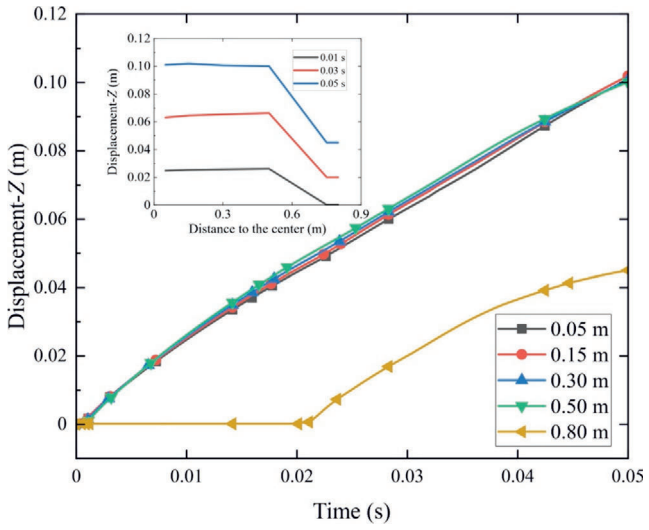

Fig. 18. Case B's Z-direction displacement time-history curve.

where the blasthole is located, and the tensile damage is mainly at the edge of the model and in the area far from the blasthole. After a period of stress wave reflection, the damage situation tends to be stable, and crush zones are formed on both sides of the central hole, and crack zones are formed on the upper circular edge of the model. Notably, the damage caused by this multiple-hole blasting process is not instant; instead, the damage occurs in approximately 2 – 3 ms, during which time the detonation stress wave reflects back and forth between the free surface and the explosive fragments until it finally stabilizes. In this work, we have not yet considered the role of explosive gas

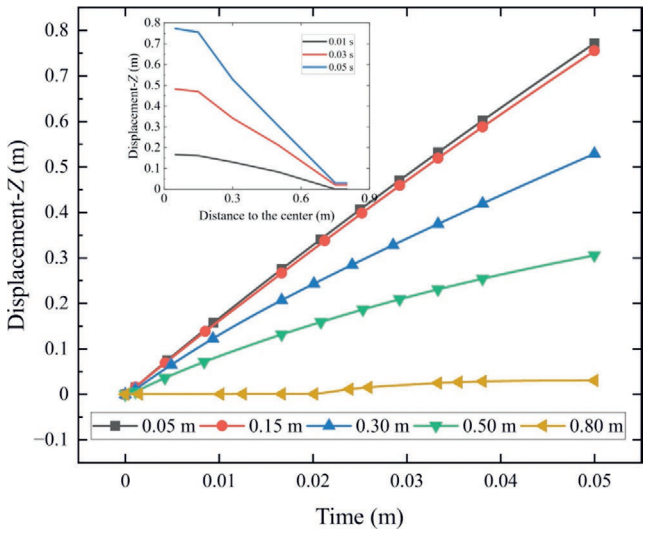

Fig. 19. Case C's Z-direction displacement time-history curve.

but have focused more on the role of explosive stress waves. This process may lead to an underestimation of the crack area. The influence of explosive gas will be a primary focus of our subsequent work.

We monitor the fracture degree (Li et al., 2013) of the model and plot the fracture degree time-history curves of the three cases, as shown in Fig. 21. The changes in the fracture degree under the three working conditions are consistent with the number of detonations. At 0.05 s, the fracture degrees of Cases A and C are basically the same at approximately 36%, whereas that of Case B is lower at only 28.65%. We determine the characteristic sizes of fragments after blasting and plot their characteristic size-grading curves as shown in Fig. 22. The blasting fragmentation characteristic size L_{bc} is calculated as follows.

$$L_{bc} = \frac{\sqrt[3]{V_f} + L_{max}}{2}, \tag{17}$$

where V_f is the volume of fragments and L_{max} is the maximum side length of the fragment.

The development trends of the three curves are basically the same, but there are differences in the local details. Considering d_{40} (the characteristic size of the fragment when the pass rate is 40%) as the evaluation index, we can see that the d_{40} values of Cases A and C are 0.3 m, whereas that of Case B is 0.63 m, which shows that there are more small fragments after the blasting of Cases A and C. Most of the fragments in Case B are medium-sized. However, d_{80}

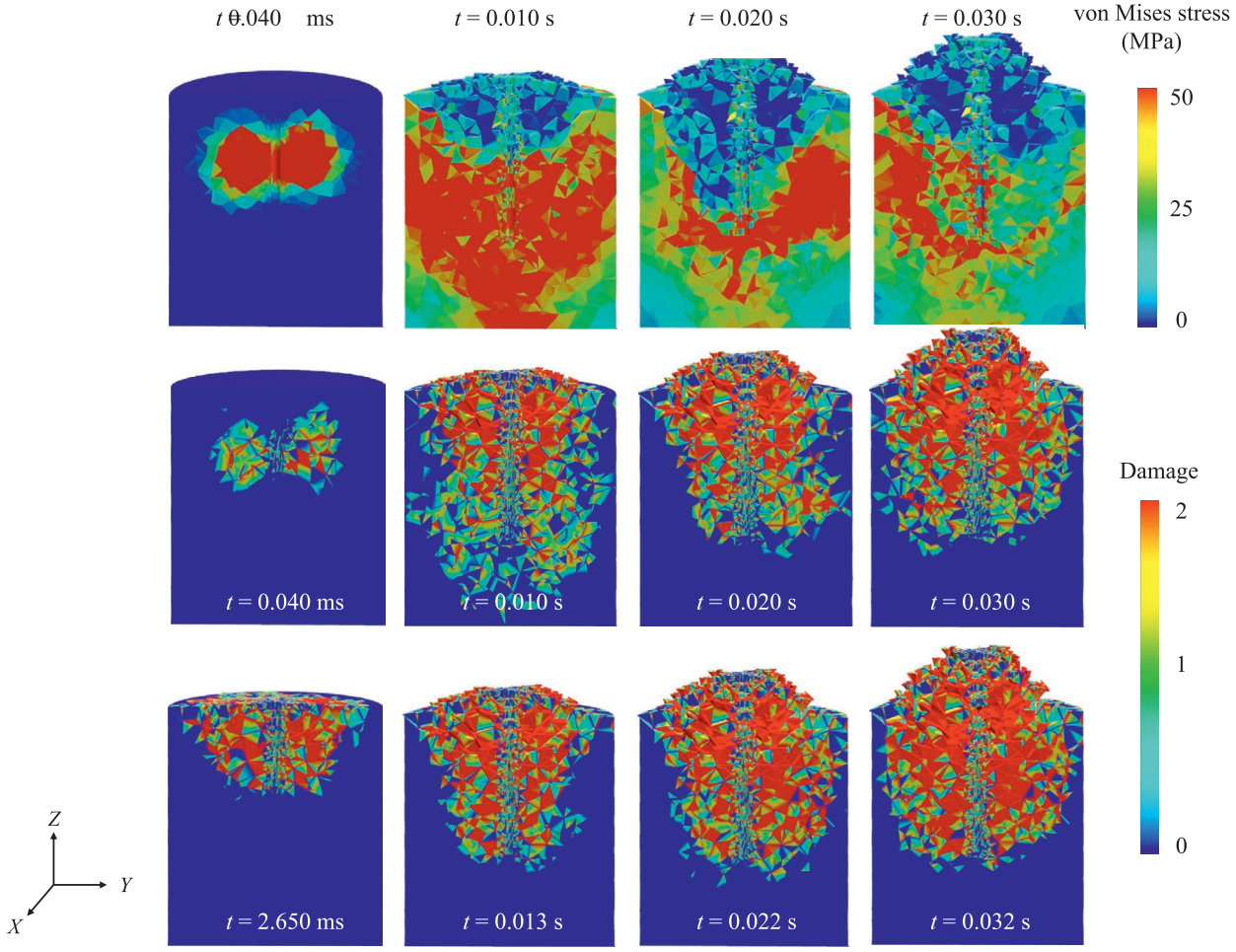

Fig. 20. Von Mises stress diagram and damage distribution of Case C.

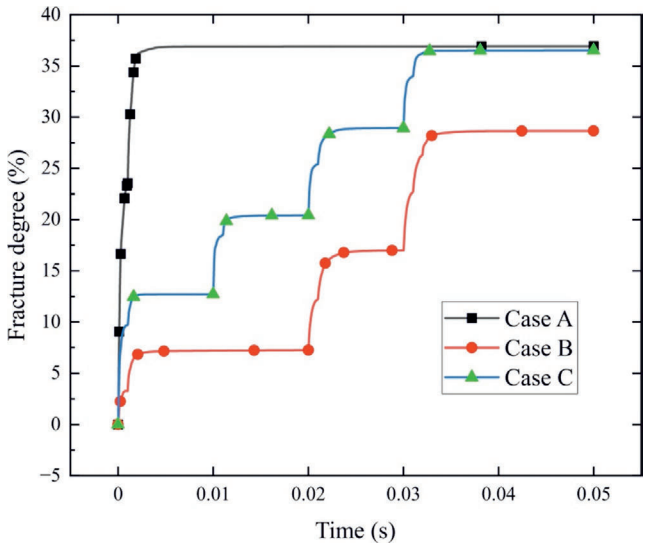

Fig. 21. Fracture degree time-history curves for three cases.

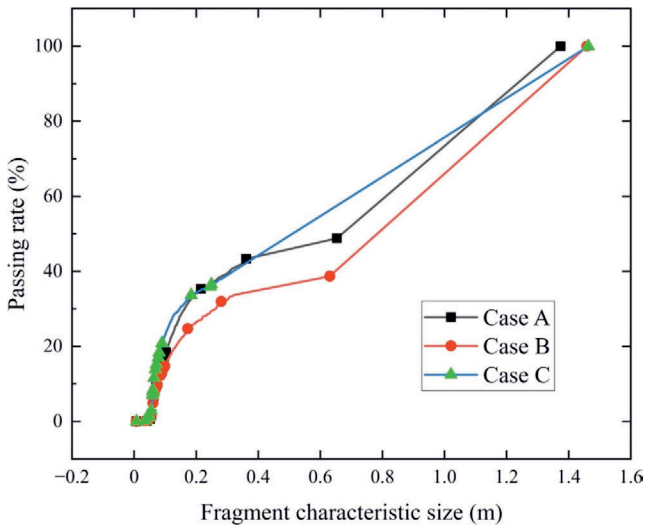

Fig. 22. Characteristic size grading curves of the fragments for the three cases.

(the characteristic size of the fragment when the pass rate is 80%) remains consistent across all three cases, measuring 1.1 – 1.2 m, demonstrating an equivalent performance for the control of large fragments.

4.2.3 Blasting funnel comparison

According to the blasting fracture of the model under the three cases, we draw the blasting funnel under the three cases and count the diameter and depth of the blasting funnel, as shown in Fig. 23. The purple zone represents the fracture funnel from the primary cut blasting in the inner circle, and yellow indicates the final blasting funnel generated by the perimeter expansion hole blasting. The red zone represents the unbroken part of the model after blasting. The shapes of the blasting funnels in the three cases are quite different. After the detonation of the inner circular blastholes in Case A, the top of the model is slightly broken, as indicated by large fragments. In Case B, the inner circle blasting results in intricate, fine cracks in the model crest (the purple zone in Case B). In stark contrast, Case C significantly overbreaks after inner-circle cut-hole blasting, with the debris appearing in a state of crushing. Compared with Cases A and B, the depth of the blasting funnel (purple zone) is basically the same at approximately 0.40 m. In terms of the shape of the blasting funnel, Case A is more elliptical, and its axial ratio e ($e = l_Y/l_X$, where l_Y denotes the Y-axis length of the inner blast funnel. l_X, which represents the X-axis length), is 1.33. However, Case B is more circular, and its axial ratio e is 1.10. Finally, the blasting footage of the three cases is basically the same at approximately 1.4 m, and that of Case C is the largest at 1.46 m. Furthermore, the blasting effect in Case C closely aligns with the engineering design expectations. This case exhibits a high degree of fracture, with the blast crater resembling a cylindrical shape. The post-blasting foundation walls maintain high structural integrity.

5 Conclusions

In this work, under the framework of the CDEM, the bar explosion model replaces conventional explicit modelling of blastholes to eliminate the computational burden caused by localized mesh refinement (blasthole zone) in solid explosive simulations while preserving the detonation accuracy of the explicit modelling. The reliability of the bar

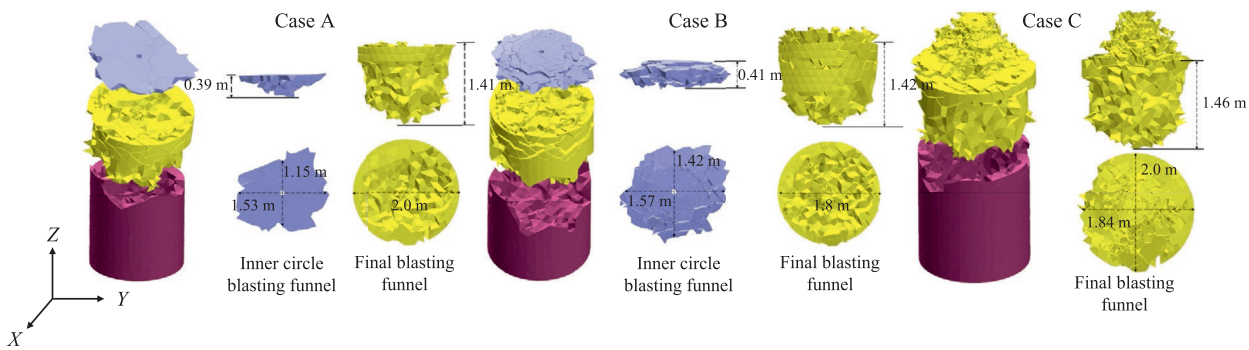

Fig. 23. Three cases of blasting funnels.

explosion model is verified by different views, such as the propagation process of explosion stress waves, damage nephograms, and explosion load time-history curves. This approach provides a reliable method for the numerical simulation of large-scale complex engineering blasting with many blastholes, such as bench and tunnel heading blasting. The main conclusions of this study are summarized as follows.

(1) Based on von Mises stress, damage nephogram, and the time-history curves of the explosion pressure, the two cases of the bar and solid explosion are compared. The propagation process of the explosion stress wave, the "swallow-like" shape of the damage nephogram, and the development trend of the explosion pressure time-history curve are all consistent with the solid explosion case, verifying the reliability of the bar explosion model.
(2) Three blasting cases of pile-foundation pit excavation are simulated using the bar explosion model combined with an engineering background. The rock fragmentation characteristics, blasting damage distribution, and fracture degree of the model are analysed in three cases, and an improved blasting scheme is provided.
(3) An analysis of three blasting cases reveals that fracture propagation in multihole blasting engineering involves a short process, with damage evolution occurring over a millisecond-scale temporal progression (duration: $2-3$ ms), whereas the scattering of fragments after blasting exhibits obvious hysteresis, which clearly changes by approximately 0.01 s after the end of detonation (one order of magnitude greater than the duration of detonation).

In this paper, we don't incorporate the effect of detonation gas into the bar explosion model; instead, we focus on using the model to reduce the computational cost of engineering-scale blasting simulations. Previously, we investigated the coupled rock-breaking action of the blasting stress wave and detonation gas using the plate flow hypothesis (Li et al., 2022). Extending that work to the bar explosion framework is the next major objective of our research.

Data availability

The data that support the findings of this study are available from the corresponding author upon reasonable request.

CRediT authorship contribution statement

Yunpeng Li: Writing – review & editing, Writing – original draft, Validation, Software, Resources, Methodology, Data curation. **Xinguang Zhu:** Software, Methodology, Formal analysis. **Dong Chen:** Funding acquisition. **Jun Fu:** Funding acquisition. **Minjie Wen:** Supervision. **Yiming Zhang:** Supervision, Funding acquisition.

Declaration of competing interest

The authors declare that they have no known competing financial interests or personal relationships that could have appeared to influence the work reported in this paper.

Acknowledgement

The authors gratefully acknowledge the financial support provided by the National Natural Science Foundation of China (Grant No. 52178324) and the Technical Development Contract of the China Railway 16th Bureau (No. WQGS-KYJS-2024-001).

References

Asadi, P., Fakhimi, A., & Javad Ashrafi, M. (2023). Dynamic tensile strength of rock specimens with different defect lengths. *Engineering Fracture Mechanics, 284*, 109245.
Durand, M., Marin, P., Faure, F., & Raffin, B. (2012). DEM-based simulation of concrete structures on GPU. *European Journal of Environmental and Civil Engineering, 16*(9), 1102–1114.
Fan, H. F., Bergel, G. L., & Li, S. F. (2016). A hybrid peridynamics - SPH simulation of soil fragmentation by blast loads of buried explosive. *International Journal of Impact Engineering, 87*, 14–27.
Feng, C., Li, S. H., Liu, X. Y., & Zhang, Y. N. (2014). A semi-spring and semi-edge combined contact model in CDEM and its application to analysis of Jiweishan landslide. *Journal of Rock Mechanics and Geotechnical Engineering, 6*(1), 26–35.
Feng, C., Zhu, X., and Wang, X. (2022). GDEM-Block Dyna (v1.0 ed.). https://support.gdem-tech.com.
Fukuda, D., Mohammadnejad, M., Liu, H. Y., Dehkhoda, S., Chan, A., Cho, S. H., Min, G. J., Han, H. Y., Kodama, J. I., & Fujii, Y. (2019). Development of a GPGPU-parallelized hybrid finite-discrete element method for modeling rock fracture. *International Journal for Numerical and Analytical Methods in Geomechanics, 43*(10), 1797–1824.
Han, H. Y., Fukuda, D., Liu, H. Y., Fathi Salmi, E., Sellers, E., Liu, T. J., & Chan, A. (2020). FDEM simulation of rock damage evolution induced by contour blasting in the bench of tunnel at deep depth. *Tunnelling and Underground Space Technology, 103*, 103495.
Henrych, J. (1979). *The dynamics of explosion and its use*. Elsevier.
Huang, X. P., Zhu, B., & Chen, Y. M. (2025). A coupled and parallel peridynamics – SPH modeling and simulation of buried explosion induced soil fragmentation and cratering. *Computers and Geotechnics, 178*, 106942.
Li, S. H., Feng, C., & Zhou, D. (2018). *Mechanics methods in landslide research*. Science Press (in Chinese).
Li, S. H., Zhou, D., & Liu, T. P. (2013). Risk analysis method of accumulated landslide based on fracture degree. *Chinese Journal of Rock Mechanics and Engineering, 32*(S2), 3909–3917 (in Chinese).
Li, Y. P., Feng, C., Ding, C. X., & Zhang, Y. M. (2022). A novel continuous-discontinuous multi-field numerical model for rock blasting. *Applied Sciences, 12*(21), 11123.
Li, Y. P., Feng, C., & Zhang, Y. M. (2023). Numerical analysis of directional rock blasting with continuous-discontinuous element method. *KSCE Journal of Civil Engineering, 27*(8), 3591–3598.
Li, Y. P., Li, J., Feng, C., Wen, M. J., & Zhang, Y. M. (2024). An interface constitutive model of plastic tensile–compressive damage under impact loading based on continuous–discontinuous framework. *Computers and Geotechnics, 173*, 106502.
Liu, Q. S., Wang, W. Q., & Ma, H. (2020). Parallelized combined finite-discrete element (FDEM) procedure using multi-GPU with CUDA. *International Journal for Numerical and Analytical Methods in Geomechanics, 44*(2), 208–238.
Lu, A., Yan, P., Lu, W. B., Li, X. F., Liu, X., Luo, S., Huang, S. L., & Grasselli, G. (2024). Crack propagation mechanism of smooth blasting

holes for tunnel excavation under high in-situ stress. *Engineering Fracture Mechanics, 304*, 110144.

Munjiza, A. (2004). Chapter 2, processing of contact interaction in the combined finite discrete element method. In *The Combined Finite-Discrete Element Method* (pp. 35–72). John Wiley & Sons Inc..

Munjiza, A., Lei, Z., Divic, V., & Peros, B. (2013). Fracture and fragmentation of thin shells using the combined finite-discrete element method. *International Journal for Numerical Methods in Engineering, 95*(6), 478–498.

Murali, G., Wong, L. S., & Abid, S. R. (2024). A comprehensive review of drop weight impact testing: Evaluating the pros and cons in fiber-reinforced concrete performance assessment. *Journal of Building Engineering, 94*, 109934.

Park, D., Jeon, B., & Jeon, S. (2009). A numerical study on the screening of blast-induced waves for reducing ground vibration. *Rock Mechanics and Rock Engineering, 42*(3), 449–473.

Saifi, F., Javaid, M., Haleem, A., & Anas, S. M. (2024). Computational fluid dynamics approach for predicting pipeline response to various blast scenarios: A numerical modeling study. *Computer Modeling in Engineering and Sciences, 140*(3), 2747–2777.

Sharafisafa, M., Aliabadian, Z., & Shen, L. M. (2025). Numerical study of presplit blasting in rock masses with a closed and filled joint using coupled finite-discrete element method. *Simulation Modelling Practice and Theory, 144*, 103199.

Xu, S. X., Wu, B., Zhang, H. L., Qi, S. X., Bian, H. B., & Wang, J. J. (2025). Directional crack propagation and optimization strategies for multi-hole shaped charge blasting in tunnel construction. *Structures, 72*, 108268.

Yin, Y., Esmaeili, K., Sun, Q., & Cao, J. (2025). Numerical investigation of rock damage induced by bilateral-groove-slot shaped charge blasting under the influence of in-situ stresses. *Computers and Geotechnics, 180*, 107070.

Zhou, H. X., Gao, Q. D., Leng, Z. D., Wang, Y. Q., Fan, Y., & Liu, G. F. (2024). Formation mechanisms of different kinds of blast-induced cracks and their extension characteristics in rock mass. *Computers and Geotechnics, 176*, 106747.

Zhu, X. G., Feng, C., Cheng, P. D., Wang, X. Q., & Li, S. H. (2021). A novel three-dimensional hydraulic fracturing model based on continuum-discontinuum element method. *Computer Methods in Applied Mechanics and Engineering, 383*, 113887.